Monthly Notices of the ROYAL ASTRONOMICAL SOCIETY

Mon. Not. R. Astron. Soc. **420,** 1553–1561 (2012) doi:10.1111/j.1365-2966.2011.20141.x

A generalized porosity formalism for isotropic and anisotropic effective opacity and its effects on X-ray line attenuation in clumped O star winds

Jon O. Sundqvist,[1★] Stanley P. Owocki,[1] David H. Cohen,[2] Maurice A. Leutenegger[3,4] and Richard H. D. Townsend[5]

[1]*Bartol Research Institute, University of Delaware, Newark, DE 19716, USA*
[2]*Department of Physics and Astronomy, Swarthmore College, Swarthmore, PA 19081, USA*
[3]*CRESST and X-ray Astrophysics Laboratory NASA/GSFC, Greenbelt, MD 20771, USA*
[4]*Department of Physics, University of Maryland, Baltimore County, 1000 Hilltop Circle, Baltimore, MD 21250, USA*
[5]*Department of Astronomy, University of Wisconsin, Madison, WI 53706, USA*

Accepted 2011 November 3. Received 2011 November 3; in original form 2011 October 2

ABSTRACT

We present a generalized formalism for treating the porosity-associated reduction in continuum opacity that occurs when individual clumps in a stochastic medium become optically thick. As in previous work, we concentrate on developing bridging laws between the limits of optically thin and thick clumps. We consider geometries resulting in either isotropic or anisotropic effective opacity, and, in addition to an idealized model in which all clumps have the same local overdensity and scale, we also treat an ensemble of clumps with optical depths set by Markovian statistics. This formalism is then applied to the specific case of bound–free absorption of X-rays in hot star winds, a process not directly affected by clumping in the optically thin limit. We find that the Markov model gives surprisingly similar results to those found previously for the single-clump model, suggesting that porous opacity is not very sensitive to details of the assumed clump distribution function. Further, an anisotropic effective opacity favours escape of X-rays emitted in the tangential direction (the 'venetian blind' effect), resulting in a 'bump' of higher flux close to line centre as compared to profiles computed from isotropic porosity models. We demonstrate how this characteristic line shape may be used to diagnose the clump geometry, and we confirm previous results that for optically thick clumping to significantly influence X-ray line profiles, very large porosity lengths, defined as the mean free path between clumps, are required. Moreover, we present the first X-ray line profiles computed directly from line-driven instability simulations using a 3D patch method, and find that porosity effects from such models also are very small. This further supports the view that porosity has, at most, a marginal effect on X-ray line diagnostics in O stars, and therefore that these diagnostics do indeed provide a good 'clumping insensitive' method for deriving O star mass-loss rates.

Key words: line: profiles – radiative transfer – stars: early-type – stars: mass-loss – stars: winds, outflows – X-rays: stars.

1 INTRODUCTION

Over the past years, it has become clear that in principle all standard spectral mass-loss diagnostics of O stars are affected by *wind clumping*, i.e. by the small-scale wind inhomogeneities that should arise naturally from a strong, intrinsic instability associated with the radiative line-driving of these winds [the line-driven instability (LDI); e.g. Owocki, Castor & Rybicki 1988]. If neglected, such wind clumping causes standard diagnostics such as Hα and infrared/radio free–free emission, which have opacities that depend on the local wind density squared, to overestimate mass-loss rates (for summaries, see Hamann, Feldmeier & Oskinova 2008; Puls, Vink & Najarro 2008).[1] The analysis here examines the degree to

[1] Diagnostic ultraviolet resonance lines, which have opacities that depend linearly on density, are directly affected by clumping only if individual clumps are *optically thick*. However, recent results indicate that clumps are indeed thick in these lines (Prinja & Massa 2010), which then can lead to reduced line strengths and *underestimates* of mass-loss rates if neglected in the analysis (Oskinova, Hamann & Feldmeier 2007; Sundqvist et al. 2011).

★E-mail: jon@bartol.udel.edu

© 2011 The Authors
Monthly Notices of the Royal Astronomical Society © 2011 RAS

Downloaded from http://mnras.oxfordjournals.org/ at NASA Goddard Space Flight Ctr on July 14, 2014

which X-ray line profiles can provide a mass-loss diagnostic that is relatively insensitive to clumping.

In single O stars without strong magnetic fields, X-rays are believed to originate in embedded wind shocks associated with the LDI (Feldmeier, Puls & Pauldrach 1997), and the broad emission lines revealed by high-resolution X-ray spectroscopy support this basic scenario (Cassinelli et al. 2001; Kahn et al. 2001; Cohen et al. 2006). These X-ray lines are often observed as blueshifted and asymmetric, characteristics stemming from attenuation by bound–free absorption in the bulk wind (MacFarlane et al. 1991). As seen by an observer, X-ray photons emitted in the receding part of the wind travel farther before escape, and thus undergo more absorption, than those emitted in the advancing part.

For optically thin clumps, the amount of bound–free absorption is proportional to the local density, and may thereby be used to put additional constraints on mass-loss rates. Whilst initial analyses (e.g. Kramer, Cohen & Owocki 2003) required very low mass-loss rates to reproduce the observed X-ray lines, more recent investigations with a better account of the wind opacity and line blends (Cohen et al. 2010, 2011a; Cohen, Wollman & Leutenegger 2011b) show that rates inferred from X-ray lines are consistent with those derived from other diagnostics, *if* clumping is adequately accounted for in the other diagnostics. However, a possible shortcoming of these X-ray analyses is the assumption that clumps are optically thin, which if not met would lead to an overestimate of the wind opacity, due to the principal effect of *porosity*.

Wind porosity models aiming to calculate X-ray line profiles have been developed by, e.g., Feldmeier, Oskinova & Hamann (2003), Oskinova, Feldmeier & Hamann (2004) and Owocki & Cohen (2006, hereafter OC06). The first two of these studies assumed the clumps to be *radially oriented*, geometrically thin shell fragments ('pancakes'), leading to a distinct anisotropic form of the effective opacity. In OC06, on the other hand, the clumps were assumed *isotropic* to impinging radiation. Whereas geometrically thin shell structures are indeed seen in 1D LDI simulations, first attempts to construct 2D LDI models suggest that these shells break up via Rayleigh–Taylor or thin shell instabilities into small clumps of similar angular and radial scales (Dessart & Owocki 2003, 2005a). But these initial 2D simulations do not yet properly treat the lateral radiation transport that might couple material, and so the degree of anisotropy of instability-generated structure in a fully consistent 3D model is still uncertain.

From the diagnostic side, OCO6 (see also Cohen, Leutenegger & Townsend 2008) argued that for porosity to significantly affect the X-ray line formation, unrealistically large porosity lengths, defined as the mean free path between clumps (see Section 3), must be invoked. This view is also supported by the above-noted recent attempts to derive mass-loss rates directly from X-ray diagnostics. On the other hand, Oskinova, Feldmeier & Hamann (2006) have argued that anisotropic clumps enhance porosity effects, and lead to more symmetric line profiles than if assuming isotropic clumps, in general agreement with X-ray observations.

This paper and its sequel (Leutenegger et al., in preparation, hereafter Paper II) further examine these issues. Building upon previous works by Owocki & Cohen (2001) and OC06, Sections 2 and 3 develop a generalized formalism for synthesizing X-ray lines, including porosity as caused by either isotropic (spherical, or randomly oriented) or anisotropic (flattened, radially oriented) clumps. In addition, we generalize our models to treat an ensemble of clumps of some distribution in optical depth, rather than retaining the assumption that all clumps are *locally* identical. Section 4 then systematically examines synthetic X-ray line profiles and analyses porosity effects for isotropic and anisotropic clumps, as well as for uniform and exponential clump distributions. We discuss how the shape of the clumps affects the line profiles in cases where porosity is important, and how this may be used to put empirical constraints on the wind's clump geometry (leaving detailed confrontation with observed spectra to Paper II). Section 5 presents first X-ray line profiles calculated directly from LDI simulations, using the 3D patch method first developed by Dessart & Owocki (2002). Section 6 gives a physical interpretation of the analytic porosity models presented, showing they can be reconciled with a general statistical model derived for stochastic transport in a two-component Markovian mixture of immiscible fluids. Finally, in Section 7 we discuss our results, compare them to other studies and give our conclusions.

2 OPACITIES IN A CLUMPED HOT STAR WIND

In our phenomenological model, we assume that the opacities in the bulk wind can be described using a two-component medium consisting of overdense 'clumps' (denoted with cl) and a rarefied 'interclump medium'. The distribution of X-ray emitters in the shock-heated wind is described in Section 3.4. We neglect the interclump medium's contribution to the opacities, an assumption well justified for absorption of X-rays in O star winds, due to the generally low X-ray optical depths found for such stars (Cohen et al. 2010, 2011a). The volume filling fraction of the dense gas is $f_{\rm V}$, thus the local mean density is $\langle\rho\rangle = f_{\rm V}\rho_{\rm cl}$, where the angle brackets denote spatial averaging.

2.1 Optically thin clumps

X-rays emitted in the wind are attenuated by bound–free absorption depending *linearly* on density. The local atomic mean volume opacity per unit length is then $\langle\chi\rangle = \kappa\langle\rho\rangle$, with mass absorption coefficient κ. By requiring that the mean density of the clumped wind be equal to the density of a corresponding smooth wind model, i.e. that $\langle\rho\rangle = \rho_{\rm sm}$, one immediately recognizes the well-known result that for atomic processes depending linearly on density, the opacities are not *directly* affected by clumping as long as the individual clumps remain optically thin. However, also linear-density opacities can via a modified wind ionization balance be *indirectly* affected by optically thin clumping, but modelling such ionization equilibria is not a focus of the present paper.

As a comparison, for processes depending on the square of the density (e.g. Hα in hot star winds), the opacities are always enhanced compared to smooth models, by a factor given by the so-called clumping factor $f_{\rm cl} \equiv \langle\rho^2\rangle/\langle\rho\rangle^2 = f_{\rm V}^{-1}$, where the latter equality holds when the interclump medium is neglected, whereby one obtains[2] $\langle\chi\rangle \propto \langle\rho^2\rangle = f_{\rm cl}\langle\rho\rangle^2 = f_{\rm V}^{-1}\rho_{\rm sm}^2$.

2.2 Porosity

It is important to realize that $\langle\chi\rangle$ may be accurately used in radiative transfer models only in the limit of optically thin clumps, $\tau_{\rm cl} \ll 1$. If this condition is not satisfied for the investigated process, the radiative transfer becomes more complex. For continuum processes such

[2] In this context, we note that the porosity formalism presented in Section 3, although developed there for the specific case of X-ray line attenuation, is applicable also for continuum processes depending on $\langle\rho^2\rangle$, for example thermal free–free emission, simply by exchanging the expression for $\langle\chi\rangle$.

Downloaded from http://mnras.oxfordjournals.org/ at NASA Goddard Space Flight Ctr on July 14, 2014

as the attenuation of X-rays considered here, optically thick clumps lead to a local self-shielding of opacity within the clumps, which in turn allows for increased escape of radiation through porous channels in between the clumps.[3] The essential effect of such *porosity* is that the 'effective' opacity of the medium becomes lower than predicted by an optically thin clump model. Thus, porosity can mimic the symmetrizing effects of reduced mass loss on the X-ray line profiles. The purpose of this paper is to present a formalism for quantifying this reduction and to show how clump geometry and distribution affect X-ray line profile morphology in the presence of porosity.

3 A POROSITY FORMALISM FOR EFFECTIVE OPACITY

In analogy with the atomic opacity, we may write the effective opacity per unit length of a clump ensemble as (e.g. Feldmeier et al. 2003)

$$\chi_{\rm eff} = n_{\rm cl} A_{\rm cl} P, \tag{1}$$

where $n_{\rm cl}$ is the number density of clumps, $A_{\rm cl}$ is the *projected* area (the geometric cross-section) of a clump for direction $\boldsymbol{n}$, and P is the probability that a photon impacting a clump gets absorbed. This probability obviously depends on the clump optical depth, $P = P(\tau_{\rm cl})$, which we here characterize by the average over all possible chord lengths ℓ through the clump for rays of direction $\boldsymbol{n}$:

$$\tau_{\rm cl} = \frac{\int \tau_\ell \, {\rm d}A_{\rm cl}}{A_{\rm cl}} = \frac{\int\int \kappa \rho_{\rm cl} \, {\rm d}\ell \, {\rm d}A_{\rm cl}}{A_{\rm cl}} = \frac{\kappa M_{\rm cl}}{A_{\rm cl}}, \tag{2}$$

where $M_{\rm cl}$ is the mass of the clump and the last equality assumes that κ is constant over the clump.

Another useful quantity is the local mean free path between clumps, also known as the porosity length h (Owocki, Gayley & Shaviv 2004):

$$h \equiv \frac{1}{n_{\rm cl} A_{\rm cl}}. \tag{3}$$

Using this definition, $\tau_{\rm cl}$ may be written as

$$\tau_{\rm cl} = \frac{\kappa M_{\rm cl}}{A_{\rm cl}} = \kappa (n_{\rm cl} M_{\rm cl}) h = \kappa \langle \rho \rangle h = \langle \chi \rangle h, \tag{4}$$

whereby

$$\chi_{\rm eff} = \frac{P(\tau_{\rm cl})}{h} \quad \Rightarrow \quad \frac{\chi_{\rm eff}}{\langle \chi \rangle} = \frac{P(\tau_{\rm cl})}{\tau_{\rm cl}}. \tag{5}$$

For $P = 1$, equation (5) returns the *atomic opacity independent* result $\chi_{\rm eff} = 1/h$, demonstrating how the porosity length h can also be interpreted as a photon's mean free path in the limit of only optically thick clumps. Further, for a constant clump density, equation (2) yields $\tau_{\rm cl} = \kappa \rho_{\rm cl} \ell_{\rm av}$, with average chord length $\ell_{\rm av}$, which then recovers the commonly used form $h = \ell_{\rm av}/f_{\rm V}$ for the porosity length.

[3] For *line* formation in a rapidly accelerating clumped medium, optically thick clumps lead to corresponding *velocity* gaps, through which line photons may escape without ever interacting with the material (Owocki 2008; Sundqvist, Puls & Feldmeier 2010). This is a consequence of the Doppler shift, leading to a picture wherein the clump length-scales can be comparable to (or even larger than) the extent of the lines' resonance zones, which is a limit wherein the porosity formalism developed here is not directly applicable.

3.1 Isotropy versus anisotropy

Note that the porosity length as defined in equation (3) is a strictly *local* quantity. And because $\tau_{\rm cl} = \langle \chi \rangle h$, this means that the (an)isotropy of the effective opacity (equation 5) depends only on $A_{\rm cl}$, and is *independent* of the spatial variation of h associated with the global wind expansion. Thus, spherical clumps (Fig. 1), as well as randomly oriented clumps of arbitrary shape, will have an isotropic effective opacity. For these cases then, assuming spherical symmetry for the global wind expansion, one may set $h = h(r)$ for all directions $\boldsymbol{n}$ impacting the clump.

However, now let us consider a specific wind model in which the clumps really are randomly distributed, but *radially oriented*, geometrically thin shell fragments ('pancakes') (Feldmeier et al. 2003; Oskinova et al. 2004). In such a model, the projected clump area is $A_{\rm cl} \boldsymbol{n} \cdot \boldsymbol{r}/|r| = A_{\mu=1}|\mu|$, where we here identify the projected area for a radially directed ray with the area for an isotropic clump (Fig. 1).

This implies the effective opacity retains its basic form (equation 5) also for such anisotropic clumps, but the clump optical depth becomes larger for oblique rays:

$$\tau_{\rm cl}(r, \mu) = \langle \chi \rangle h(r, \mu) = \langle \chi \rangle h(r)/|\mu|, \tag{6}$$

where the isotropic case is recovered by setting $\mu = 1$, and the radial dependencies of the mean opacity and directional cosine have been suppressed. This paper considers only isotropic and 'pancake' geometries, but the porosity formalism outlined above applies generally to any clump geometry described by $A_{\rm cl} = f(\boldsymbol{n})$, where f is some function.

To illustrate such isotropic versus anisotropic absorbing media, Fig. 2 compares a random distribution of spherical clumps and radially oriented pancakes, as illuminated by a uniform background source (see Appendix A). Note that for visual clarity, we extend these visualizations only to an outer radius $5R_*$. We stress that Fig. 2 is for general illustration purposes; the uniform background illumination is not a distribution of X-ray emitters. Also, we repeat that though assumed in the visualizations, spherical clumps are actually not a necessity for obtaining isotropic porosity; the requirement for this is rather that the clumps be randomly oriented (see above).

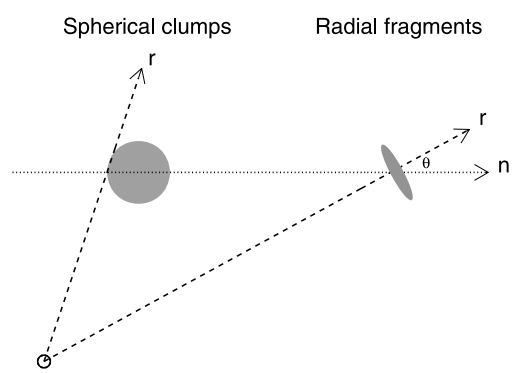

Figure 1. Schematic of photon of direction $\boldsymbol{n}$ impacting a spherical clump and a radially oriented ($\boldsymbol{r}/|r|$) shell fragment. The former gives an isotropic effective opacity, whereas the latter gives an anisotropic effective opacity, since the projected surface area depends on direction cosine $\mu \equiv \cos\theta = \boldsymbol{n} \cdot \boldsymbol{r}/|r|$.

© 2011 The Authors, MNRAS **420,** 1553–1561
Monthly Notices of the Royal Astronomical Society © 2011 RAS

Downloaded from http://mnras.oxfordjournals.org/ at NASA Goddard Space Flight Ctr on July 14, 2014

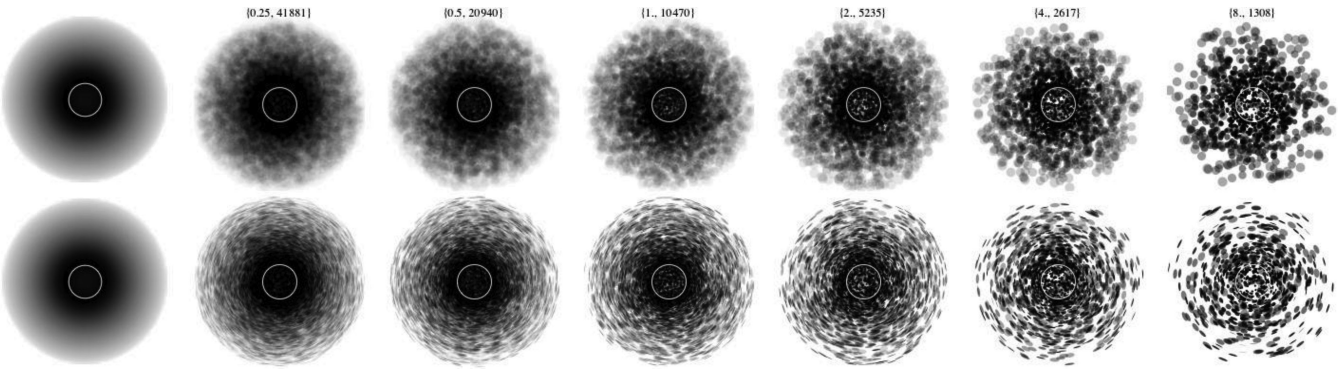

Figure 2. Back-lit rendition of randomly generated spherical (upper row) and radially compressed (lower row) clumps in a spherically expanding structured wind (columns 2–7), compared to a back-lit smooth wind (column 1) with $\tau_\star = 1$ and the same total mass between an onset radius $1.05R_\star$ and a maximum visualization radius $5R_\star$. The terminal porosity length $h_\infty/R_\star$ increases from left to right, as given by the left header, but clump diameters all scale as $d_{\rm cl} = (0.2/\sqrt{\pi})r$. The right header gives the total number of clumps. The white circle represents the star, which also radiates with the same surface brightness as the background source. Appendix A gives details on how these visualizations were generated.

3.2 Bridging laws for the effective opacity

For attenuation with a given local clump optical depth $\tau_{\rm cl} = \tau_0$, let us assume that the probability of absorption simply takes the basic form $P = 1 - {\rm e}^{-\tau_0}$. While formally exact only in cases where all chord lengths across the clump are equal, this expression is a suitable approximation that yields with equation (5):

$$\frac{\chi_{\rm eff}}{\langle\chi\rangle} = \frac{1 - {\rm e}^{-\tau_0}}{\tau_0}. \tag{7}$$

This 'single-clump' bridging law now has the correct values in the limiting cases; it returns the atomic mean opacity when $\tau_0 \ll 1$ and is independent of it when $\tau_0 \gg 1$. And as discussed in the preceding section, the bridging law equation applies for both isotropic and anisotropic effective opacity models, however with different expressions for the clump optical depth.

Assuming the effective mean free path scales as $\chi_{\rm eff}^{-1} = \langle\chi\rangle^{-1} + h$, an even simpler 'inverse' (or 'Rosseland'; see OC06) bridging law was invoked in OC06:

$$\frac{\chi_{\rm eff}}{\langle\chi\rangle} = \frac{1}{1 + \tau_0}, \tag{8}$$

which also has the correct optically thin and thick limits. By considering the *direction-dependent* mean free path, this inverse bridging law can be realized also for anisotropic models.

In OC06, the practical motivation for invoking equation (8) was because the optical depth integral for X-ray attenuation could then be solved analytically. However, Section 6 shows it also happens to represent the bridging law that follows from assuming that the local clump optical depth distribution function obeys Markovian statistics. Thus, the single-clump and inverse bridging laws (equations 7 and 8) differ in that the former assumes all clumps have the same local optical depth (for a given direction), whereas the latter averages over an exponential distribution in $\tau_{\rm cl}$.

3.3 Velocity stretch porosity

OC06 assumed that the porosity length scales with the local radius, but for mass-conserving clumps such a scaling is only appropriate for isotropic expansion. For clumps released into a radially expanding stellar wind, the wind acceleration will 'stretch' the clump spacing in proportion to the wind velocity (Feldmeier et al. 2003). The analysis here assumes this velocity stretch form for both isotropic and anisotropic porosity.

This distinction is most easily seen for the radially fragmented shell model, in which the average radial separation between two shells is $\Delta r = h(r)$. For shells moving radially according to a 'β-velocity law', $w(r) = v(r)/v_\infty = (1 - R_\star/r)^\beta$, where $R_\star$ is the stellar radius, the separation is $h(r) = h_\infty w(r)$, with the parameter h_∞ representing the asymptotic radial separation as $w \to 1$. For simplicity, this paper assumes the prototypical value $\beta = 1$. The quantity h_∞/v_∞ represents the average time between two consecutive shell passings at a fixed radial point in the wind (Sundqvist et al. 2010), which may also be interpreted as the inverse of a 'fragmentation frequency' n_0 (Oskinova et al. 2004, 2006). For example, $h_\infty = R_\star$ gives a fragmentation frequency $n_0 = v_\infty/R_\star$ that is equal to the inverse of the wind flow time.

3.4 X-ray line transfer in porosity models

To compute X-ray emission line profiles, we solve the standard formal integral of radiative transfer, using a customary (p, z) coordinate system and following the basic procedure described in Owocki & Cohen (2001) for the distribution of X-ray emitters. Since our primary interest here is the *shapes* of the lines, all resulting flux profiles have been normalized to a unit maximum, $\mathcal{F}_{\rm x}^{\rm norm} = \mathcal{F}_{\rm x}/{\rm Max}(\mathcal{F}_{\rm x})$. For simplicity, we assume that the X-ray emission begins at a certain onset radius $R_0 = 1.5R_\star$, and is constant beyond it. This onset radius is consistent with that typically predicted by conservative, self-excited LDI simulations (Runacres & Owocki 2002), and both $R_0 \approx 1.5R_\star$ and a constant X-ray filling factor are supported by observations (Cohen et al. 2006, 2011a; Leutenegger et al. 2006). Moreover, both LDI simulations and the observed X-ray luminosities indicate that only a very small mass fraction, less than 1 per cent, of the stellar wind is shock heated to X-ray-emitting temperatures at any given time. Simulations and observed lack of X-ray variability further indicate that there are numerous sites of X-ray emission distributed throughout the wind, justifying our assumption of a smoothly distributed X-ray-emitting plasma above the onset radius. Note, though, that R_0 does not necessarily equal the clump onset radius $R_{\rm cl}$, which observations typically indicate is located much closer to the photosphere (Puls et al. 2006; Cohen et al. 2011a; see also Fig. 2 for a visualization). But in

Downloaded from http://mnras.oxfordjournals.org/ at NASA Goddard Space Flight Ctr on July 14, 2014

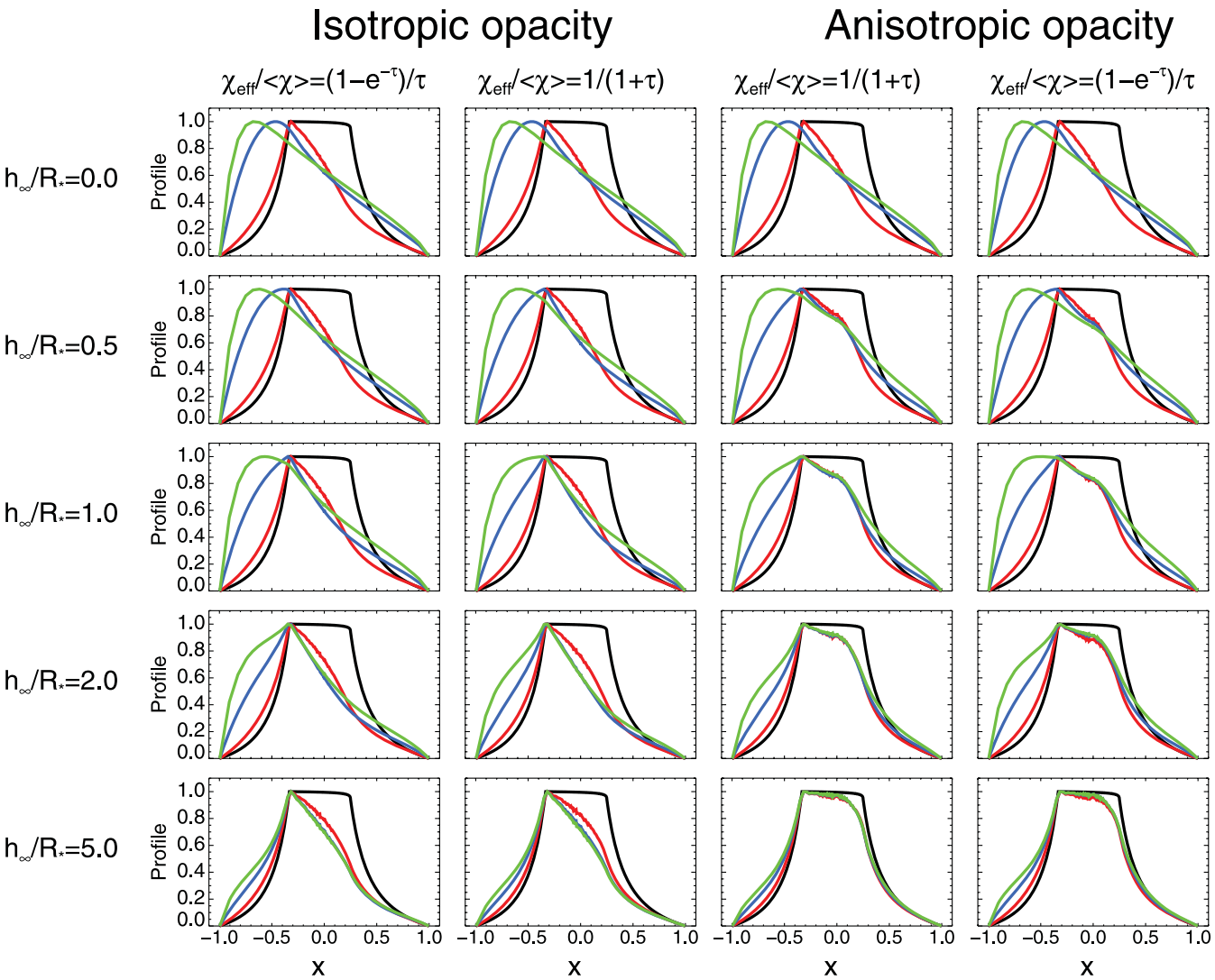

Figure 3. Synthetic X-ray line profiles for the 'single clump', $\chi_{\rm eff}/\langle\chi\rangle = (1-{\rm e}^{-\tau})/\tau$, and the 'inverse', $\chi_{\rm eff}/\langle\chi\rangle = 1/(1+\tau)$, effective opacity bridging laws and for different porosity length parameters, $h_\infty/R_\star$, as labelled. All models assume an onset radius for the X-ray emission $R_0 = 1.5R_\star$. The abscissae display the dimensionless wavelength $x = (\lambda/\lambda_0 - 1)c/v_\infty$, with λ_0 the line-centre wavelength, and the ordinates display the normalized flux. Black, red, blue and green dashed lines have an optical depth parameter $\tau_\star = 0.01$, 1, 5 and 10, respectively; for a non-colour separation, an increased $\tau_\star$ means a more blueshifted peak flux. Note that we have set $h_\infty = 0$ (the uppermost panel) to be equivalent to assuming only optically thin clumps.

the velocity stretch porosity models, we have verified that the exact value of this $R_{\rm cl}$ is not important for the resulting X-ray line profiles.

The absorption of X-rays emitted at position $z_{\rm e}$ along a ray with impact parameter p is given by the optical depth integral:

$$\tau(p, z_{\rm e}) = \int_{z_{\rm e}}^{\infty} \chi_{\rm eff}(z, p)\,{\rm d}z, \tag{9}$$

where the *effective* opacity accounts for any porosity. The opacity in a smooth or optically thin clump model, due purely to the atomic mean opacity $\langle\chi\rangle$, is proportional to the mass-loss rate $\dot{M}$ of the star and here characterized by a fiducial optical depth $\tau_\star = \dot{M}\kappa/(4\pi R_\star v_\infty)$, with wind terminal speed v_∞. To evaluate equation (9) for our porosity models, the only additional input parameter required is the porosity length h (see equations 4–8). This holds for isotropic as well as anisotropic effective opacity models, and for the single-clump as well as the inverse bridging laws.[4]

4 X-RAY LINE PROFILES FROM ANALYTIC POROSITY MODELS

Fig. 3 displays synthetic X-ray line profiles calculated using the four possible combinations of isotropic versus anisotropic effective opacity and single-clump versus inverse bridging laws. The figure clearly shows that profiles calculated using the two different bridging laws are very similar (see also Fig. 5, as well as fig. 1

[4] Source codes to all X-ray line porosity models presented in this section are publicly available at (package WINDPROF) http://heasarc.gsfc.nasa.gov/docs/xanadu/xspec/models/wind prof.html, where models for the broad-band absorption of X-rays (package WINDTABS; Leutenegger et al. 2010) also can be found.

Downloaded from http://mnras.oxfordjournals.org/ at NASA Goddard Space Flight Ctr on July 14, 2014

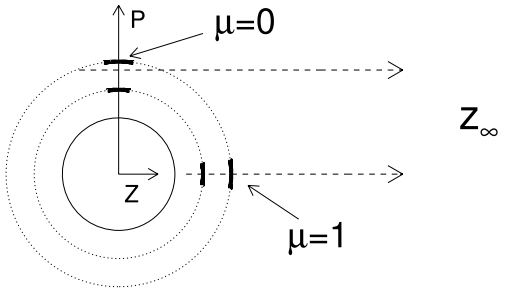

Figure 4. Illustration of the 'venetian blind' effect seen in porosity models using an anisotropic effective opacity. The dashed arrowed lines represent two different p-rays and the observer is assumed to be located at z_∞.

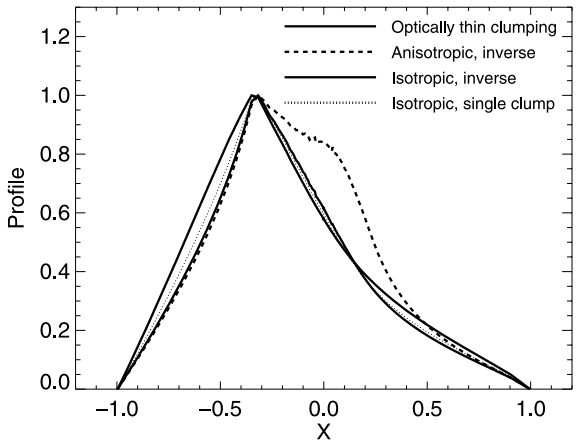

Figure 5. Line profiles for $h_\infty = R_\star$ and $\tau_\star = 2.5$, using different effective opacity laws, as labelled.

in OC06), despite representing two very different clump optical depth distributions (Section 3.2). This indicates that the effects of porosity on X-ray line profiles are not very sensitive to the specific local distribution in $\tau_{\rm cl}$. We discuss this important result further in Section 6.

The second key feature of Figs 3 and 5 is the prominent 'bump' visible close to line centre in profiles calculated with anisotropic effective opacity. Conceptually, we may understand this as a 'venetian blind' effect (Fig. 4; see also Feldmeier et al. 2003); since the fragmented shells are radially oriented, the blinds are closed for radial photons, but open up for more tangential ones. This leads to increased escape for photons emitted close to line centre, since the line emission wavelength scales with direction cosine μ as $x = -\mu w$ (e.g. Owocki & Cohen 2001).

Another way to look at this effect is to consider the optical depth integral for anisotropic effective opacity in the $\tau_{\rm cl} \gg 1$ limit:

$$\tau(p, z) = \int_{z_{\rm e}}^{\infty} \chi_{\rm eff}(z, p)\,{\rm d}z \approx \int_{z_{\rm e}}^{\infty} \frac{|\mu|}{h(r)}{\rm d}z, \qquad (10)$$

which shows that, since ${\rm d}r = \mu\,{\rm d}z$, the optical depth in this limit is set simply by counting up the number of porosity lengths. In the plane-parallel limit of radially oriented, geometrically thin but optically thick fragments, *all* tangential ($\mu = 0$) photons would escape. However, due to sphericity effects (i.e. that μ increases as the photon propagates through the wind), also photons emitted initially in the tangential direction will suffer some absorption (see Fig. 4). Thus, the end result is not complete transmission, but a characteristic bump stemming from the reduced integrated optical depth for photons emitted around $x \approx 0$. For isotropic porosity, on the other hand, no μ factor enters in equation (10), and therefore no bump appears in these profiles.

This quite distinct and *systematic* difference in the shape around line centre between models with isotropic and anisotropic effective opacity is a key result of the present analysis. Indeed, one can use this difference to set empirical constraints on the clump geometry by confronting synthetic X-ray spectra with observed ones, as will be done in Paper II.

Generally, Fig. 3 confirms earlier results by OC06 that in order to achieve a significant effect on the profiles, rather large porosity lengths, $h_\infty > R_\star$, are required. However, Fig. 5 reveals that for a value of $\tau_\star = 2.5$, representative of the prototypical O supergiant ζ Pup (Cohen et al. 2010), the anisotropic porosity model displays significantly higher flux around line centre than the other profiles, also for $h_\infty = R_\star$. Further comparisons show that, for the parameters used in Fig. 5, the isotropic porosity model is well matched by a corresponding optically thin clump model with $\tau_\star$ reduced by ~ 20 per cent (a detailed quantification of this trade-off will be provided in Paper II). In contrast, such a simple optical depth reduction does not reproduce the line-centre region in anisotropic porosity models, i.e. there is no simple trade-off, or degeneracy, between mass-loss rate and anisotropic porosity. Thus, whereas it will be difficult to distinguish between optically thin clumps and moderate isotropic porosity with somewhat higher $\tau_\star$ values, careful line-fitting to observations should be able to identify, or refute, an anisotropic porosity.

Finally, for very large porosity lengths, giving $\tau_{\rm cl} \gg 1$ in a large portion of the wind, the profile shapes do indeed become quite independent of atomic opacity. In the bottom panel of Fig. 3, profiles computed using an anisotropic effective opacity are actually very similar to the flat-topped profiles stemming from computations without any X-ray absorption, whereas profiles computed using an isotropic effective opacity retain a certain degree of asymmetry. This result differs from that found in OC06, wherein very near symmetry was achieved for isotropic profiles with very large porosity lengths, and comes about due to the $h \propto v$ scaling adopted here, which implies significantly shorter porosity lengths in the lower wind regions than the $h \propto r$ used in OC06. However, for more moderate values of h_∞ (top three panels in Fig. 3), all profiles are opacity-dependent, as expected since in the formation of these lines, porosity is a secondary effect.

5 X-RAY LINE PROFILES FROM LDI SIMULATIONS

The above simplified analytic models demonstrate that the effect of optically thick clumps on wind continuum absorption can be well characterized in terms of the wind porosity length, parametrized here by the asymptotic value h_∞ and assuming a radial variation set by the velocity stretch form, $h(r) = h_\infty(1 - R_\star/r)$ (Section 3.3).

But inspection of LDI simulations suggests a substantially steeper radial variation for the separation between instability-generated wind clumps. Even in 1D models in which the separation can become of the order of a stellar radius in the outer wind (implying $h_\infty \approx R_*$), the initial clump structure formed near the onset radius $r \approx 1.5R_*$ tends to have a much smaller separation scale, of the order of the Sobolev length $L_{\rm sob} \approx (v_{\rm th}/v)R_* \approx 0.01R_*$, where $v_{\rm th}$ is the ion thermal velocity. The sharp increase in separation from this onset comes not just from velocity stretching from the

Downloaded from http://mnras.oxfordjournals.org/ at NASA Goddard Space Flight Ctr on July 14, 2014

overall wind acceleration, but also from *collisional merging* of clumps with substantial radial velocity dispersion. For a given asymptotic porosity length h_∞, LDI models thus tend to have smaller inner-wind porosity lengths than assumed in the simple velocity stretch scaling. Since it is in this inner wind region that clumps can become optically thick for X-rays, this suggests that LDI models will show even weaker porosity effects than implied by the analytic profiles shown in Figs 3 and 5. To demonstrate this explicitly, we now present some first sample calculations of X-ray profiles computed from 1D LDI simulations that are phased randomly among 3D patches of a parametrized angular size (as first developed in Dessart & Owocki 2002). The details of this patch geometry as implemented in our radiative transfer code are given in Sundqvist et al. (2011). Here we adapt this code to synthesize X-ray line profiles by making the following assumptions. The X-ray emission is assumed to have a fixed spatial form independent of wind structure, scaled in proportion to the density squared of a smooth 'CAK' wind and with an onset radius $R_0 = 1.5R_*$. The bound–free absorption is then calculated directly from the structured LDI simulation presented in Sundqvist et al. (2011) (computed following Feldmeier et al. 1997).

Fig. 6 plots X-ray line profiles for the same wind optical depth used for analytic models in Fig. 5, namely $\tau_* = 2.5$. The curves compare a smooth CAK model to structured LDI models with patch sizes of 1° and 3°. The overall shapes agree well with corresponding non-porous analytic models, except for small differences due to the fact that the CAK velocity law does not exactly follow the phenomenological $\beta = 1$ law. However, the key point is that the LDI profiles are very similar to the CAK profile, implying little porosity effect; however, we note that for a 3° patch size, there is a small, but notable, 'bump' around line centre, presumably associated with the anisotropic (pancake) nature of the clumped structure in such models.

These results confirm that porosity is as marginal in LDI simulations as in corresponding analytic stretch porosity models with comparable asymptotic clump separations (i.e. $h_\infty \approx R_\star$). Moreover, in 2D LDI models (Dessart & Owocki 2003, 2005a), clumps can also be broken up by shearing and associated effects, leading generally to more, smaller, and less optically thick clumps, characterized by even smaller porosity lengths. Future work will implement our radiative transfer tools also in such genuinely multidimensional instability models.

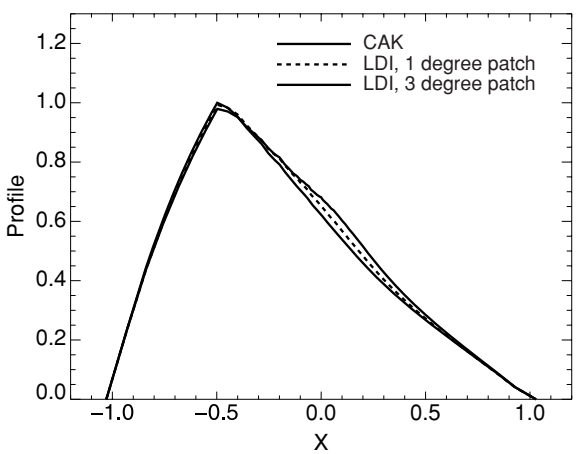

Figure 6. Line profiles for $\tau_\star = 2.5$, calculated from a smooth CAK model and structured LDI models with patch sizes 1° and 3° (see text), as labelled.

6 A PHYSICAL INTERPRETATION OF THE EFFECTIVE OPACITY BRIDGING LAWS

As already noted, a basic difference between the two bridging laws adopted in this paper is that one (equation 7, the 'single-clump' law) assumes a locally constant clump optical depth for all clumps, whereas the other (equation 8, the 'inverse' law) represents a certain distribution in $\tau_{\rm cl}$. Before discussing porosity effects on the synthetic X-ray line profiles in Section 7, this section examines the nature of this distribution.

6.1 Distribution laws for $\tau_{\rm cl}$

To investigate how a distribution of clump optical depths affects effective opacity scalings, let us assume that the ratio of the effective to the mean opacity scales as the ratio of an effective clump optical thickness to its mean:

$$\frac{\chi_{\rm eff}}{\langle\chi\rangle} = \frac{\tau_{\rm eff}}{\langle\tau\rangle} = \frac{\int_0^\infty \tau f(\tau)\frac{1-{\rm e}^{-\tau}}{\tau}{\rm d}\tau}{\int_0^\infty \tau f(\tau)\,{\rm d}\tau}, \tag{11}$$

where for clarity we have dropped the indices on the clump optical depths. Equation (11) introduces $f(\tau)$, the normalized distribution function of clumps, and $\tau_{\rm eff}$, the distribution weighted mean of the clump optical depth. Selecting a weighing function $(1-{\rm e}^{-\tau})/\tau$ ensures that the single-clump bridging law (equation 7) is recovered from equation (11) when the distribution function is a Dirac delta function, $\delta(\tau - \tau_0)$.

Let us now choose a specific distribution function of the exponential form:

$$f(\tau) = \frac{{\rm e}^{-\tau/\tau_0}}{\tau_0}, \tag{12}$$

which has a mean value τ_0. Using equation (12) in equation (11) yields directly the inverse bridging law equation (8), but with τ_0 now only representing the *mean* clump optical depth, rather than a unique one as in the exponential bridging law equation (7). Again, despite the large difference between this clump distribution and the one assuming a constant τ, the two bridging laws give similar results, as demonstrated in Section 4.

6.2 Connecting Markovian statistics to exponentially distributed clumps

We now show that the bridging law resulting from this exponential distribution turns out to be a special case of a general scaling derived for a stochastic mixture of two fluids that follow Markovian statistics (e.g. Levermore, Wong & Pomraning 1988; Pomraning 1991). The Markov assumption is that the future state of the system only depends on its present state, and not on its history. Along any given ray through the medium, if the fluid is of component 0 at location s, the probability of it being of component 1 at $s + {\rm d}s$ is $P_{0,1}{\rm d}s$, where $P_{0,1}$ is independent of how far back along the ray the last transition (from fluid 1 to 0) occurred. Under this assumption, the length-scales travelled within the fluid components are random variables described by the Poisson distributions, with $P_{0,1}$ identified as the inverse of ℓ_0, the *mean* distance a photon travels along the ray in fluid 0 before finding itself in component 1. A similar definition applies for ℓ_1.

For such a two-component Markov model with opacities χ_0 and χ_1, Levermore et al. (1988) derived for the effective opacity in the pure absorption case:

$$\chi_{\rm eff} = \frac{\langle\chi\rangle + \chi_0\chi_1\ell_{\rm c}}{1 + (p_0\chi_1 + p_1\chi_0)\ell_{\rm c}}, \tag{13}$$

Downloaded from http://mnras.oxfordjournals.org/ at NASA Goddard Space Flight Ctr on July 14, 2014

where $p_i \equiv \ell_i/(\ell_0 + \ell_1)$, $\langle\chi\rangle = p_0\chi_0 + \chi_1 p_1$ is the mean opacity, and $\ell_c \equiv \ell_0\ell_1/(\ell_0 + \ell_1)$ is the correlation length (Pomraning 1991). Identifying the clumps in our model with component 1, and assuming the interclump medium to be void ($\chi_0 = 0$), we find for this 'clump+void Markov model'

$$\frac{\chi_{\rm eff}}{\langle\chi\rangle} = \frac{1}{1 + p_0\chi_1\ell_c} = \frac{1}{1 + \langle\chi\rangle p_0\ell_0} = \frac{1}{1 + \langle\chi\rangle h}. \quad (14)$$

Here p_0 represents the probability that a photon is in the void medium, while ℓ_0 is the distance the photon travels in the void before encountering a clump; the product $p_0\ell_0$ thus represents the photon mean free path in the case of optically thick clumps, which is also the porosity length h, as given by the final equality in equation (14). Comparison with equation (8) then shows that the effective opacity bridging law for an exponential clump optical depth distribution is equivalent to that for this statistical clump+void Markov model.

Indeed, recalling that the Markov transport is defined along a given ray, we may make the same identification for the anisotropic porosity model, with the photon mean free path along the ray then being scaled by $1/|\mu|$.

6.3 Exponentially truncated power-law distributions

While there are not many observational constraints on the distribution of clumps in a hot star wind (see, however, Lépine & Moffat 1999; Dessart & Owocki 2005b), the above identification with the Markov model at least places our porosity models on a robust and well-known statistical ground. The inverse bridging law should therefore be an appropriate standard choice for porosity applications such as the X-ray line formation considered here, but perhaps also for, e.g., porosity-moderated continuum-driven wind models of stars formally exceeding the Eddington luminosity, as investigated by Owocki et al. (2004). Indeed, although not explicitly studied in that paper, we note that the Markov model represents a special case of the exponentially truncated power-law distribution of clumps considered in Owocki et al. (2004), namely the one with power index $\alpha_p = 2$. Thus, reasonable extensions of the two canonical distributions studied here could readily be done by using some other power index variant given in Owocki et al. (2004).

7 DISCUSSION AND CONCLUSIONS

7.1 Isotropy or anisotropy

Let us next compare our analysis to that by Oskinova et al. (2006). These authors also pointed out the differences between isotropic and anisotropic effective opacity and carried out a comparison, however only for the specific case of $\tau_\star = 10$ and a fragmentation frequency (see Section 3.3) $n_0 = 1.4 \times 10^{-4}\,{\rm s}^{-1}$. Taking the parameters for the O supergiant ζ Pup adopted in Oskinova et al., this corresponds to $h_\infty = v_\infty/n_0 = 4.24\,R_\star$, which in turn roughly corresponds to the bottom panel in our Fig. 3. Indeed, the profiles displayed in that panel agree well with those in fig. 16 of Oskinova et al.; both figures illustrate that for such very large porosity lengths, profiles computed using anisotropic effective opacity are nearly symmetric (Section 4).

This comparison suggests an overall good agreement among the results found by the different groups. However, as shown in Section 4, anisotropic porosity line profiles, with their characteristic 'bump' at line centre, are qualitatively different from isotropic porosity or optically thin clumping profiles. Thus, the good statistical fits presented for ζ Pup by Cohen et al. (2010), without invoking porosity, seem somewhat contradictory to the good visual fits presented by Oskinova et al. (2006), using models with moderate anisotropic porosity $h_\infty \approx R_\star$. Paper II will further examine and quantify these differences between anisotropic porosity on the one hand, and isotropic porosity or optically thin clumping on the other.

7.2 Is porosity important for X-ray line mass-loss diagnostics?

The LDI simulations presented in Section 5 indicate small porosity lengths and negligible porosity effects on X-ray line profiles. Such small porosity lengths also have some indirect empirical support. Namely, the mass-loss rate derived for ζ Pup by Cohen et al. (2010), without invoking porosity, is only marginally lower than the *upper limit* mass-loss rate derived by Puls et al. (2006), by assuming an unclumped outermost radio-emitting wind, while allowing for clumping in the intermediate and lower wind. Because of the trade-off between porosity and mass-loss rate then, if porosity lengths large enough to significantly affect the X-ray line profiles were to be adopted, $h_\infty > R_\star$, the inferred X-ray mass-loss rate would be *higher* than this upper limit. That is, such multiwavelength considerations indicate that a significant porosity effect on X-ray-based mass-loss rates is incompatible with diagnostic results from other wavebands.

Overall, we thus conclude that porosity effects on X-ray line profiles are likely to be, at most, a marginal effect in typical O stars. This is supported also by the low optical depths found for ζ Pup as well as for the even denser wind of HD 93129A (Cohen et al. 2010, 2011a). Since most O stars will have characteristic $\tau_\star$ values significantly lower than these, porosity effects should be negligible. The upshot is that X-ray line analysis may indeed provide the best available 'clumping insensitive' diagnostic of O star mass-loss rates.

ACKNOWLEDGMENTS

This work was supported in part by NASA ATP grant NNX11AC40G. DHC acknowledges support from NASA ADAP grant NNX11AD26G to Swarthmore College. We thank A. Feldmeier for providing the instability simulations discussed in Section 5, and for suggesting the exploration of Markov models discussed in Section 6.

REFERENCES

Cassinelli J. P., Miller N. A., Waldron W. L., MacFarlane J. J., Cohen D. H., 2001, ApJ, 554, L55
Cohen D. H., Leutenegger M. A., Grizzard K. T., Reed C. L., Kramer R. H., Owocki S. P., 2006, MNRAS, 368, 1905
Cohen D. H., Leutenegger M. A., Townsend R. H. D., 2008, in Hamann W.-R., Feldmeier A., Oskinova L. M., eds, Clumping in Hot-Star Winds. Universitätsverlag Potsdam, Potsdam, p. 209
Cohen D. H., Leutenegger M. A., Wollman E. E., Zsargó J., Hillier D. J., Townsend R. H. D., Owocki S. P., 2010, MNRAS, 405, 2391
Cohen D. H., Gagné M., Leutenegger M. A., MacArthur J. P., Wollman E. E., Sundqvist J. O., Fullerton A. W., Owocki S. P., 2011a, MNRAS, 415, 3354
Cohen D. H., Wollman E. E., Leutenegger M. A., 2011b, in Neiner C., Wade G., Meynet G., Peters G., eds, IAU Symp. Vol. 272, Active OB Stars: Structure, Evolution, Mass Loss, and Critical Limits. Cambridge Univ. Press, Cambridge, p. 348
Dessart L., Owocki S. P., 2002, A&A, 383, 1113
Dessart L., Owocki S. P., 2003, A&A, 406, L1
Dessart L., Owocki S. P., 2005a, A&A, 437, 657

Downloaded from http://mnras.oxfordjournals.org/ at NASA Goddard Space Flight Ctr on July 14, 2014

Dessart L., Owocki S. P., 2005b, A&A, 432, 281
Feldmeier A., Puls J., Pauldrach A. W. A., 1997, A&A, 322, 878
Feldmeier A., Oskinova L., Hamann W.-R., 2003, A&A, 403, 217
Hamann W.-R., Feldmeier A., Oskinova L. M., eds, 2008, Clumping in Hot-Star Winds. Universitätsverlag Potsdam, Potsdam
Kahn S. M., Leutenegger M. A., Cottam J., Rauw G., Vreux J.-M., den Boggende A. J. F., Mewe R., Güdel M., 2001, A&A, 365, L312
Kramer R. H., Cohen D. H., Owocki S. P., 2003, ApJ, 592, 532
Lépine S., Moffat A. F. J., 1999, ApJ, 514, 909
Leutenegger M. A., Paerels F. B. S., Kahn S. M., Cohen D. H., 2006, ApJ, 650, 1096
Leutenegger M. A., Cohen D. H., Zsargó J., Martell E. M., MacArthur J. P., Owocki S. P., Gagné M., Hillier D. J., 2010, ApJ, 719, 1767
Levermore C. D., Wong J., Pomraning G. C., 1988, J. Math. Phys., 29, 995
MacFarlane J. J., Cassinelli J. P., Welsh B. Y., Vedder P. W., Vallerga J. V., Waldron W. L., 1991, ApJ, 380, 564
Oskinova L. M., Feldmeier A., Hamann W.-R., 2004, A&A, 422, 675
Oskinova L. M., Feldmeier A., Hamann W.-R., 2006, MNRAS, 372, 313
Oskinova L. M., Hamann W.-R., Feldmeier A., 2007, A&A, 476, 1331
Owocki S. P., 2008, in Hamann W.-R., Feldmeier A., Oskinova L. M., eds, Clumping in Hot-Star Winds. Universitätsverlag Potsdam, Potsdam, p. 121
Owocki S. P., Cohen D. H., 2001, ApJ, 559, 1108
Owocki S. P., Cohen D. H., 2006, ApJ, 648, 565 (OC06)
Owocki S. P., Castor J. I., Rybicki G. B., 1988, ApJ, 335, 914
Owocki S. P., Gayley K. G., Shaviv N. J., 2004, ApJ, 616, 525
Pomraning G. C., 1991, Linear Kinetic Theory and Particle Transport in Stochastic Mixtures. Universitätsverlag Potsdam, Potsdam
Prinja R. K., Massa D. L., 2010, A&A, 521, L55
Puls J., Markova N., Scuderi S., Stanghellini C., Taranova O. G., Burnley A. W., Howarth I. D., 2006, A&A, 454, 625
Puls J., Vink J. S., Najarro F., 2008, A&AR, 16, 209
Runacres M. C., Owocki S. P., 2002, A&A, 381, 1015
Sundqvist J. O., Puls J., Feldmeier A., 2010, A&A, 510, A11
Sundqvist J. O., Puls J., Feldmeier A., Owocki S. P., 2011, A&A, 528, A64

APPENDIX A: GENERATION METHOD FOR CLUMPED MEDIUM ILLUSTRATIONS

The clumped medium illustrations in Fig. 2 were generated by following the radial expansion of mass-conserving clumps. As with the analogous illustration in fig. 3 of OC06, we assume the clump scale l increases in proportion to the local radius:

$$l(r) = l_* \frac{r}{R_*} \,. \tag{A1}$$

However, instead of the OC06 assumption of a purely isotropic ('Hubble law') velocity expansion $v \sim r$, we now use a standard $\beta = 1$ wind velocity law. For clumps of projected area $A_{\rm cl} = l^2 \propto r^2$ and local volume density $n_{\rm cl} \propto 1/(v\, r^2)$, this gives the associated radial variation of the porosity the desired 'velocity-stretch' form:

$$h(r) = \frac{1}{n_{\rm cl} A_{\rm cl}} = h_\infty \frac{v(r)}{v_\infty} = h_\infty (1 - R_*/r) \,. \tag{A2}$$

For specified clump parameters l_* and h_∞, the clump number density is thus given by

$$n_{\rm cl}(r) = \frac{1}{h A_{\rm cl}} = \frac{v_\infty R_*^2}{h_\infty l_*^2} \frac{1}{r^2 v(r)} \,. \tag{A3}$$

Note that, unlike the OC06 isotropic expansion model, the clump volume filling factor in this velocity-stretch scaling is *not constant*, but varies spatially as $f_{\rm V} \propto n_{\rm cl} l^3 \propto r/v(r)$, which actually is quite consistent with derived observational constraints (e.g. Puls et al. 2006).

The cumulative number of clumps up to a radius r above the clump onset radius $R_{\rm cl}$ is

$$N(r) = 4\pi \int_{R_{\rm cl}}^{r} n_{\rm cl} r'^2 \, {\rm d}r' = \frac{4\pi R_*^3}{h_\infty l_*^2} \left[\frac{r - R_{\rm cl}}{R_*} + \ln\left(\frac{r - R_*}{R_{\rm cl} - R_*} \right) \right] . \tag{A4}$$

For a specified outer radius $R_{\rm max}$, the total number of clumps is $N_{\rm tot} = N(R_{\rm max})$. Since Fig. 2 uses fixed parameters $l_*/R_* = 0.1$, $R_{\rm cl}/R_* = 1.05$ and $R_{\rm max}/R_* = 5$, this number scales with $1/h_\infty$, and ranges from $N_{\rm tot} = 1308$ for the largest porosity length $h_\infty/R_* = 8$ in the rightmost column, to $N_{\rm tot} = 41\,881$ for the least porous case $h_\infty/R_* = 0.25$ in column 2.

A random set of $N_{\rm tot}$ clumps with the required statistical distribution in radius can now be drawn simply by generating a set of pseudo-random numbers $\mathcal{R}_{\rm i}$ over the range [0, 1], and inverting the normalized cumulative distribution function $F(r) \equiv N(r)/N_{\rm tot} = \mathcal{R}_{\rm i}$ to find the radius r:

$$r(\mathcal{R}_{\rm i}) = R_* \left(1 + {\rm ProductLog}[\exp(C_{\rm cl} + C_{\rm max} \mathcal{R}_{\rm i})]\right) \,, \tag{A5}$$

with the constants given by

$$C_{\rm cl} = R_{\rm cl}/R_* - 1 + \ln(R_{\rm cl}/R_* - 1), \tag{A6}$$

$$C_{\rm max} = (R_{\rm max} - R_{\rm cl})/R_* + \ln\left(\frac{R_{\rm max} - R_*}{R_{\rm cl} - R_*} \right) . \tag{A7}$$

Likewise, we use the assumed statistical spherical symmetry and generate the clump angle coordinates in azimuth ϕ and colatitudinal cosine μ through additional pseudo-random numbers:

$$\phi_i = 2\pi \mathcal{R}_{i+N_{\rm tot}} \,; \quad \mu_i = 2\mathcal{R}_{i+2N_{\rm tot}} - 1 \,. \tag{A8}$$

In this system, it is most convenient to assume that the clumps are viewed from above the $\mu = 1$ pole, thus with $\mu > 0$ ($\mu < 0$) representing clumps in the foreground (background) hemisphere.

With the random set of clump positions in hand, the clump sizes are set by equation (A1), with all cases in Fig. 2 using $l_*/R_* = 0.1$. To give the associated projected area $l^2 = A_{\rm cl} = \pi d_{\rm cl}^2/4$, the clump diameters are set to $d_{\rm cl} = 2l/\sqrt{\pi}$.

For the spherical clumps in the upper row of Fig. 2, the transparency of each individual projected clump disc area is set by $\exp(-\tau_{\rm cl})$, where the surface-averaged clump optical depth is $\tau_{\rm cl} = \tau_* h_\infty R_*/r^2$. For the radially compressed clumps in the lower row, the associated clump optical depths are increased by $1/|\mu|$; their projected areas are reduced through foreshortening their radial extent by a factor of $|\mu|$, while keeping their radially perpendicular extent equal to the local clump diameter $d_{\rm cl}$.

Finally, clumps in the back hemisphere ($\mu < 0$) that are behind the star (with $r\sqrt{1-\mu^2} < R_*$) are simply not drawn. This effectively means the clumps directly in front of the star appear as if illuminated by a stellar surface brightness equal to the back illumination of the clumps outside the stellar limb.

This paper has been typeset from a TEX/LATEX file prepared by the author.

Downloaded from http://mnras.oxfordjournals.org/ at NASA Goddard Space Flight Ctr on July 14, 2014